Universal metabolic constraints on the thermal tolerance of marine phytoplankton

Samuel Barton[1*], James Jenkins[1], Angus Buckling[1], C.-Elisa Schaum[1], Nicholas Smirnoff[2] & Gabriel Yvon-Durocher[1*]

[1] Environment and Sustainability Institute, University of Exeter, Penryn Campus, Penryn, Cornwall TR10 9EZ, UK,

[2] Biosciences, College of Life and Environmental Sciences, Geoffrey Pope Building University of Exeter, Exeter, EX4 4QD, UK

*for correspondence, email: G.Yvon-Durocher@exeter.ac.uk , sb384@exeter.ac.uk

Abstract

Marine phytoplankton are responsible for over 45% of annual global net primary production. Ocean warming is expected to drive massive reorganisation of phytoplankton communities, resulting in pole-ward range shifts and sharp declines in species diversity, particularly in the tropics. The impacts of warming on phytoplankton species depend critically on their physiological sensitivity to temperature change, characterised by thermal tolerance curves. Local extinctions arise when temperatures exceed species' thermal tolerance limits. The mechanisms that determine the characteristics of thermal tolerance curves (e.g. optimal and maximal temperatures) and their variability among the broad physiological diversity of marine phytoplankton are however poorly understood. Here we show that differences in the temperature responses of photosynthesis and respiration establish physiological trade-offs that constrain the thermal tolerance of 18 species of marine phytoplankton, spanning cyanobacteria as well as the red and green super-families. Across all species we found that rates of respiration were more sensitive to increasing temperature and typically had higher optimal temperatures than photosynthesis. Consequently, the fraction of photosynthetic energy available for allocation to growth (carbon-use efficiency) declined exponentially with rising temperatures with a sensitivity that was invariant among the 18 species. Furthermore, the optimal temperature of growth was generally lower than that of photosynthesis and as a result, supra-optimal declines in growth rate were associated with temperature ranges where the carbon-use efficiency exhibited accelerated declines. These highly conserved patterns demonstrate that the limits of thermal tolerance in marine phytoplankton are underpinned by common metabolic constraints linked to the differential temperature responses of photosynthesis and respiration.

Significance Statement

The impacts of warming on marine phytoplankton depend on their sensitivity to rising temperatures, yet there is currently limited understanding of the mechanisms that limit thermal tolerance among the diversity of marine phytoplankton. Using a comparative study on the dominant, ecologically important lineages of marine phytoplankton – Bacillariophyceae, Dinophyceae, Cyanophyceae, Prasinophyceae, Prymnesiophyceae – we

49 show that rates of respiration are consistently more sensitive to increasing temperature than

50 photosynthesis. Consequently, the fraction of photosynthetic energy available for growth

51 declines with rising temperatures with a sensitivity that is invariant among species. Our

52 results suggest that declines in phytoplankton performance at high temperatures are driven by

53 universal metabolic constrains linked to rising respiratory costs eventually exceeding the

54 supply of reduced carbon from photosynthesis.

55

Introduction

56

57 The planet's oceans are changing at an unprecedented rate (1); over the past half-

58 century average sea surface temperatures have been increasing by 0.1 ℃ per decade (2) and

59 are projected to rise by a further 3℃ or more by the end of the century (3). Ocean warming is

60 thought to be a key driver of recent declines in phytoplankton productivity (4–6), and models

61 of marine biogeochemistry predict further reductions in productivity over the 21st century as

62 temperatures exceed limits of thermal tolerance and nutrient limitation increases in warmer,

63 more stratified oceans (7). Thermal tolerance curves of marine phytoplankton (like all

64 ectotherms) exhibit characteristic unimodality and left-skew, meaning that fitness declines

65 more sharply above the optimum temperature than below (8). Marine phytoplankton species

66 exhibit substantial variability in their thermal tolerance. Optimal temperatures for growth

67 range between approximately 2 to 38℃ and are positively correlated with the average

68 temperature of the environment, indicating a global pattern of thermal adaptation (8, 9).

69 Ocean warming is expected to result in major reorganisation of marine phytoplankton

70 communities as temperatures exceed the thermal optima of some species but not others. In

71 particular, tropical and sub-tropical regions are projected to experience pronounced declines

72 in species diversity and productivity (8, 9) because many of the taxa in these areas already

73 exist close to their limits of thermal tolerance. Despite its importance for predicting the

74 impacts of global warming on marine phytoplankton communities, we currently understand

75 very little about the physiological processes that determine the limits of thermal tolerance in

76 marine phytoplankton.

77 To address this fundamental knowledge gap we carried out a large-scale experiment

78 to investigate the physiological mechanisms that set the limits of thermal tolerance in marine

79 phytoplankton. Our experiments span a representative sample of the broad physiological and

80 phylogenetic diversity of the marine phytoplankton; including 18 species belonging to

81 ecologically important functional groups – Cyanobacteria, Diatoms, Dinoflagellates,
82 Coccolithophores, Rhodophytes, Chlorophytes and Prasinophytes (Table 1, SI). These
83 species were chosen to encompass the putative primary and secondary endosymbionts of both
84 the red and green super-families, and thus reflect the complex evolutionary histories of
85 marine phytoplankton (10, 11). This allowed for us to investigate whether, in spite of such
86 physiological diversity in plastid evolution, similar physiological constraints underpin the
87 limits of thermal tolerance.

88

89 Results & Discussion

90   We first characterised variability in thermal tolerance curves among taxa by
91 measuring growth rates for each species across a temperature gradient spanning 15 to 37°C
92 and fitting the Sharpe-Schoolfield equation for high temperature inactivation to the data using
93 non-linear mixed effects modelling (12, 13) (Fig.1). The upper limits of thermal tolerance
94 varied across the taxa, with T_{max}^{μ} (maximum temperature of observed growth), ranging from
95 27°C to 37°C. The optimal temperature of growth, T_{opt}^{μ}, ranged from 23.8°C to 34.0°C and
96 the activation energy, E_a^{μ} – which characterises the increase in rate up to T_{opt}^{μ} – ranged from
97 0.40 eV to 1.46 eV, with an average E_a^{μ} of 0.77eV (95% CI: 0.58 to 0.97) (Fig.1, and Table
98 2, SI). These E_a^{μ} values highlight that the temperature dependence of growth at the species
99 level is significantly higher than previously reported temperature dependence parameters,
100 such as the canonical Eppley coefficient (equivalent to $E_a^{\mu} \approx 0.3$ eV), that are derived by
101 comparing maximum growth rates across many species and are the standard way in which the
102 impacts of warming on phytoplankton productivity are represented in models of marine
103 biogeochemistry (14–16). These findings suggest that the Eppley coefficient (and other
104 values from similar analyses (16)), which capture the broad-scale, macroecological impacts
105 of temperature along geographic gradients, might significantly under estimate the impacts of
106 temperature fluctuations on phytoplankton growth at local to regional scales (see
107 Supplementary Information : additional text, S1, for further discussion).

108   To determine the physiological processes that shape the thermal tolerance curves, in
109 particular those that determine the optimum temperature and supra-optimal declines in
110 growth rate, it is essential to understand how the key metabolic pathways that drive biomass
111 synthesis respond to warming. Despite having diverse evolutionary histories, all unicellular

112   phytoplankton share common, key metabolic pathways (17) and their ability to sequester

113   carbon, and therefore grow, is ultimately determined by photosynthesis and respiration (18,

114   19). The light-dependent reactions of photosynthesis account both for the processes that

115   convert inorganic carbon to organic carbon stores and those that facilitate the production of

116   ATP and reductant used to fuel biomass synthesis (20). The dark reactions in respiration can

117   be conceptually divided into 'growth' and 'maintenance' components (18–21). 'Growth-

118   respiration' provides the ATP, reductant and carbon skeletons required for producing new

119   biomass and is expected to be proportional to the rate of growth. By contrast, 'maintenance-

120   respiration' provides the ATP for macromolecular turnover and the maintenance of solute

121   gradients, and is proportional to cell biomass (20). Whilst dark respiration clearly plays an

122   important role in photolithotrophic growth in microalgae, the majority of the energy used to

123   fuel biosynthesis (between $60 - 90\%$) is thought to derive from photosynthesis (20, 21). To

124   understand the physiological constraints that shape the variability in phytoplankton thermal

125   tolerance, we quantified temperature-dependent variation in rates of photosynthesis and dark

126   respiration in the 18 species of marine phytoplankton.

127   For each species, we measured the acute responses of gross photosynthesis and dark

128   respiration across a temperature gradient spanning 7°C to 49°C, and quantified the resultant

129   thermal response curves by fitting the Sharpe-Schoolfield equation for high temperature

130   inactivation to the data using non-linear mixed effects modelling (see Methods). We found

131   consistent differences in the parameters characterising the thermal responses of

132   photosynthesis and respiration across all the species in this study despite their diverse

133   evolutionary histories (Fig.2, Fig.3 and 4, SI). The activation energy for respiration was

134   greater than that of photosynthesis (i.e. $E_a^R > E_a^P$; Fig. 3B, Fig. 3 and 4, SI) in all 18

135   species. Pooling the parameters across species yielded an average activation energy for

136   photosynthesis of $E_a^P = 0.74$ eV (95% CI: 0.69 to 0.79), whilst the average for respiration was

137    $E_a^R = 1.07$ eV (95% CI: 0.98 to 1.15). Critically, the average activation energy for

138   photosynthesis was statistically indistinguishable from that of growth rate ($E_a^\mu = 0.77$eV, 95%

139   CI: 0.58 to 0.97). These results demonstrate that respiratory costs become an increasingly

140   large proportion of photosynthetic carbon fixation and biomass synthesis as temperatures rise

141   toward the peak of the thermal response curves. We also found that for most species, the

142   optimum temperature for respiration was higher than that of photosynthesis (i.e. $T_{opt}^R >$

143   T_{opt}^P), with the average thermal optimum for photosynthesis, $T_{opt}^P = 31.18$°C ± 0.83 (s.e.m.)

144   and respiration, $T_{opt}^R = 32.91$°C ± 0.48 (s.e.m.) (Fig. 3C, Fig. 3 and 4, SI). Furthermore, in

145   all species, the deactivation energy, which characterises the speed that rates decline past the

146   optimum, was lower for respiration relative to photosynthesis (i.e. $E_h^P > E_h^R$), with the

147   average across species for photosynthesis $E_h^P = 6.08$ (95% CI: 5.04 to 7.12) and respiration

148   $E_h^R = 2.62$ (95% CI: 2.31 to 2.93) (Fig. 3D, Fig. 3 and 4, SI). Thus, as temperatures rise

149   beyond T_{opt}, rates of photosynthesis decline faster than rates of respiration. Overall these

150   findings show remarkable consistency across diverse taxa (Fig. 3 and 4, SI) in how

151   differences in the parameters that characterise the thermal responses of photosynthesis and

152   respiration result in increasing respiratory expenditure of carbon fixed by photosynthesis as

153   temperatures rise.

154   The carbon-use efficiency (CUE = 1-R/P), is an estimate of the fraction of

155   photosynthetic energy (P) that can be allocated to growth after accounting for respiration (R).

156   Recent work on both marine and freshwater phytoplankton species suggests that declines in

157   CUE at high temperature may be linked to impaired performance at supra-optimal

158   temperature (22, 23). Furthermore, observations that the evolution of elevated thermal

159   tolerance are coupled with adaptive shifts in metabolic traits that increase CUE at high

160   temperature (22–24), imply an important role for CUE in constraining thermal tolerance that

161   could provide a general explanation for high-temperature impairment of growth across the

162   diversity of the phytoplankton. To determine whether the differential thermal responses of

163   photosynthesis and respiration can help explain the physiological processes that constrain the

164   thermal tolerance curves of diverse phytoplankton, we quantified how the CUE varied as a

165   function of temperature. Consistent with previous work, we found that the CUE decreased

166   with increasing temperature in all 18 species. Declines in the CUE with rising temperature

167   were however highly non-linear, with the fall in CUE dramatically accelerating at high

168   temperatures. Because $T_{opt}^R > T_{opt}^P$ and $E_h^P > E_h^R$ for most species, as temperature rose

169   beyond T_{opt}^P the CUE exhibited an accelerated decline at high temperatures. To quantify this

170   non-linear response and the location of the inflection point where declines in CUE become

171   accelerated, we fitted a break-point model to the thermal responses of the CUE. We found a

172   significant break-point in the thermal response of the CUE for all 18 species that was tightly

173   coupled with T_{opt}^P (Fig.3). As $E_a^R > E_a^P$ for all species, temperature dependent declines in

174   CUE up to the break-point were universal across the species (Fig.4) with an average

175   activation energy, E_a^{CUE}, of -0.12eV (95% CI: -0.16 to -0.08). Furthermore, in all 18 species

176   the optimum temperature for growth (T_{opt}^μ) either coincided with the CUE break-point (i.e.

177   the 95% CIs of the CUE break-point included $T_{opt}{}^{\mu}$), or was lower than the CUE break-point

178   (Fig.3). This finding suggests that temperature-driven declines in the CUE, linked to

179   fundamental differences in the intrinsic thermal responses of photosynthesis and respiration,

180   could play an important role in constraining the thermal tolerance of diverse marine

181   phytoplankton. Because the metabolic costs for repair and maintenance are largely accounted

182   for by dark respiration (20, 21) the temperature-driven declines in the CUE likely reflect

183   increases in the costs associated with maintenance and repair of heat-induced cellular damage

184   that eventually exceed the rate of substrate supply by photosynthesis, causing rates of growth

185   to decline at supra-optimal temperatures.

186   It is important to note that our experiments were conducted under nutrient replete

187   conditions. A recent study has suggested that the temperature sensitivities of photosynthesis

188   and respiration (25) in some marine phytoplankton may decline under nutrient limitation and

189   that the differential temperature sensitivities of photosynthesis and respiration may be

190   negligible under limited conditions. This work however quantified the temperature

191   sensitivities of photosynthesis and respiration at only 3 or 4 temperatures leading to estimates

192   of thermal sensitivities with large error margins and a high probability of generating type II

193   errors (i.e. accepting the null hypothesis of no difference in the thermal sensitivity of

194   photosynthesis and respiration). Furthermore, measurements were made only under resource

195   limited conditions precluding a quantitative comparison with nutrient replete conditions via

196   the same methodology. Whilst we expect that the absolute values of the thermal sensitivities

197   of photosynthesis and respiration are likely to decline under resource limitation, it is highly

198   improbable that the intrinsic differences between photosynthesis and respiration documented

199   in this study under nutrient replete conditions will be erased under nutrient limitation. Indeed,

200   our analyses demonstrate that light limitation had a negligible impact on the temperature

201   sensitivity of photosynthesis and in particular, the fundamental differences in the impacts of

202   temperature on photosynthesis and respiration were preserved under light limited conditions

203   (see Fig.2 and Table 6, SI). We therefore anticipate that the supra-optimal declines in growth

204   linked to temperature-driven decoupling between photosynthesis, respiration and biomass

205   synthesis that we have shown here, apply equally under nutrient replete and limited

206   conditions. Whilst large areas of the global ocean are under nutrient limited conditions for

207   long periods (26), understanding the impacts of temperature under nutrient replete conditions

208   (as we have done here) remains critically important because a large proportion of marine

209   primary productivity occurs during episodic bloom events driven by short periods of

210 increased nutrient concentrations (27–29). Clearly, significant further work is required to

211 understand the interplay between temperature and nutrient availability on phytoplankton

212 physiology and to assess whether the patterns we have shown here apply to conditions of

213 nutrient limitation, given that current experimental evidence (25) is not sufficient to draw

214 meaningful conclusions.

215

Conclusions

216

217 Overall, our findings highlight marked similarities in the temperature dependence of

218 photosynthesis and respiration across diverse taxonomic groups, spanning the cyanobacteria

219 and red and green super families and suggest that common physiological trade-offs underpin

220 the thermal tolerance of marine phytoplankton. We found that rates of respiration were more

221 sensitive to temperature, had higher thermal optima and declined less abruptly past the

222 optimum than those of photosynthesis. Consequently, the fraction of photosynthetic energy

223 available for allocation to growth (the CUE) exhibited an accelerated decline with rising

224 temperatures in a manner that was highly conserved among the 18 species investigated. We

225 also found that the optimal temperature for growth coincided with, or was lower than, an

226 inflection point in the temperature dependence of the CUE, which marked a transition that led

227 to accelerated declines at high temperatures. These patterns suggest that universal metabolic

228 constraints driven by the differential temperature sensitivity of photosynthesis and respiration

229 play a key role in setting the limits of thermal tolerance of diverse marine phytoplankton. Our

230 results therefore help pave the way for improving representations of phytoplankton

231 biodiversity in models of ocean biogeochemistry by providing a process-based understanding

232 of the factors that shape the limits of temperature tolerance for diverse species of marine

233 phytoplankton, which can be used to aid predictions of immigration and local extinctions

234 driven by global warming.

235

Methods

236

Culturing of marine phytoplankton strains

237

238 18 marine phytoplankton strains were obtained from CCAP (The Culture Collection of Algae

239 and Protozoa) and RCC (Roscoff Culture Collection) between autumn 2015 and spring 2016.

240   Strains of eukaryotic phytoplankton were selected from phylogenetic groups of both the red

241   and green superfamilies (10, 11), in addition to two strains of cyanobacteria. We tried to

242   work with organisms that had been well studied in the literature, were known to be globally

243   abundant and play crucial roles for marine ecology and global carbon cycling. The strains

244   were originally isolated from a range of latitudes and some have been in culture for up to 65

245   years (Table 1, SI). Stocks of each of the strains were cultured on their previous culture

246   collection medium (Table 1, SI) using artificial sea water. The following media were used:

247   Guillard's F/2 and F/2 + Si, Keller's K, K + Si and K/2, and PCR-S11 Red Sea medium (with

248   Red Sea salts). All stock cultures were incubated in Infors HT incubators at 20°C, under a

249   12:12 hour light-dark cycle with a PAR intensity of 45-50 µmol m^{2}s^{-1} and shaken at 65RPM.

250   Where possible we tried to obtain strains from the culture collections that matched, or were

251   close to, these conditions. The red alga *Porphyridium purpureum* was an exception, which we

252   cultured at 20-25 µmol m^{2}s^{-1}. Cultures were kept under exponential, nutrient replete, growth

253   conditions for ~ 2 months before any physiological data was collected.

254

Measuring the thermal tolerance curve

256   For each species, a minimum of 3 technical replicates were inoculated with the same starting

257   density into fresh growth medium across a range of temperatures (15°C - 37°C). Cell counts

258   were made daily using flow cytometry (Accuri C6 flow cytometer, BD Scientific), and

259   population density was tracked until cultures reached carrying capacity. Per capita growth

260   rates (μ) were quantified from a modified Baranyi growth model without the lag phase(30),

261   using non-linear least squares regression via the 'nlsMicrobio' package in R statistical

262   software (v3.3.1). Models were fitted using the 'nlsLoop' function in the R github package

263   'nlsLoop'. This draws on the 'nlsLM' function in the 'minpack.lm' R package, which uses a

264   modified Levenberg-Marquardt optimisation algorithm. Model parameters were determined

265   by running 2000 random combinations of estimated starting parameters, which were then

266   selected using the Akaike Information Criterion (AIC) to determine the set of parameters that

267   best characterised the data. Growth rates derived for each technical replicate at each growth

268   temperature were then used to determine the thermal tolerance curves (Fig.1A).

Estimates of Cell Carbon and Nitrogen

270   For each species, an exponentially growing culture from the 20°C stock was divided into 3

271   technical replicates and centrifuged at 3500RPM, at 4°C for 30 minutes. The resultant pellets

272   were rinsed with deionised water and re-spun 3 times to remove any artificial sea water

273   residue. For the calcifying organisms (*Emiliania huxleyi, Gephyrocapsa oceanica,*

274   *Thoracosphaera heimii* i.e. those with a calcium carbonate coccoliths) it was necessary to

275   dissolve the extra-cellular inorganic carbon (31, 32). This was achieved by treating these

276   pellets with 0.5 mL of 3M HCl for 1 hour before being rinsed with deionised water and re-

277   pelleted. All pellets were freeze-dried using a CoolSafe (95-15 PRO, ScanVac) over 24 hours

278   and then weighed to obtain dry weight. Samples were placed in tin cups and sent to Elemtex

279   (Elemtex Ltd, Cornwall, UK, PL17 8QS) for elemental analysis of %C and %N using a

280   SerCon Isotope Ratio Mass Spectrometer (CF-IRMS) system (continuous flow mode). For

281   each technical replicate we then calculated the C:N ratio as well as $\mu g\ C\ cell^{-1}$ (Table 3, SI).

282

Measuring the metabolic thermal response curves

284   Measurements of photosynthesis and dark respiration were collected across a range of assay

285   temperatures (7°C to 49°C) for a minimum of 3 biological replicates per species. We used a

286   clark-type oxygen electrode as part of a Chlorolab 2 system (Hansatech Ltd, King's Lynn,

287   UK) to measure net rates of oxygen evolution in the light (net primary production, NP) and

288   oxygen consumption in the dark (dark respiration); both in units of $\mu mol\ O_2\ mL^{-1}\ s^{-1}$. All

289   biological replicates were sampled from the stock cultures, which had all been growing at

290   20°C and were taken at the mid-logarithmic growth phase to ensure that the samples were not

291   substrate limited. To improve the signal to noise ratio when measuring rates, all biological

292   replicate samples were concentrated by centrifugation at 1500rpm, 20°C, for 15 minutes and

293   re-suspended into an adequate volume of fresh growth medium. Prior to running a sample at

294   each assay temperature, all samples were given ~ 15 minutes to pre-acclimate to the assay

295   temperature in the dark before any data was collected. This also gave the electrode system

296   sufficient time to stabilise before metabolic rates were measured. This was necessary for two

297   reasons, i) as the sample adjusts to the assay temperature this will naturally cause changes in

298   the dissolved oxygen concentration, ii) the electrode system results in oxygen signal drift, and

299   this too is temperature dependent. We measured rates of oxygen depletion from 21 sterilised

300   artificial seawater samples across a range of temperatures 4°C - 44°C and found that the

301   impact of drift was minimised after ~15 minutes of stabilisation time. Nevertheless, signal

302   drift was linearly temperature dependent after this time. To account for drift in our dataset we

303   corrected all our raw data using the following empirically derived relationship:

304 $$drift = (-0.392 \times T) - 6.51 \qquad\qquad [1]$$

305 Where T is assay temperature (°C), and *drift* is the non-biological depletion in oxygen

306 concentration measured in units $\mu mol O_2 \; mL^{-1} \; s^{-1}$ after approximately 15 minutes of

307 stabilisation. The raw O_2 flux data was then corrected by subtracting the estimated drift.

308 Rates of net photosynthesis, measured as O_2 evolution, were collected across a range of light

309 intensities from 0 to 1800 $\mu mol \; m^2 \; s^{-1}$ with increments of 50 $\mu mol \; m^2 \; s^{-1}$ between 0 to 200

310 $\mu mol \; m^2 \; s^{-1,}$ 100 $\mu mol \; m^2 \; s^{-1}$ between 200 and 1000 $\mu mol \; m^2 \; s^{-1}$, followed by 1200 $\mu mol \; m^2 \; s^{-}$

311 ^{1}, 1500 $\mu mol \; m^2 \; s^{-1}$ and finally 1800 $\mu mol \; m^2 \; s^{-1}$. This enabled us to model a photosynthesis-

312 irradiance (PI) curve for each assay temperature, and therefore obtain an estimate of light

313 saturated net photosynthesis, NP_{max}, see Eq. 2. Respiration (R) was measured as oxygen

314 consumption in the dark, over a 3-minute period directly following the light response outlined

315 above. The photosynthesis-irradiance curve was then quantified by fitting Eiler's

316 photoinhibiton model to the data using non-linear least squares regression (as described

317 above) (33, 34):

318 $$NP(I) = \frac{NP_{max}I}{\frac{NP_{max}}{\alpha I_{opt}^2}I^2 + \left(1 - 2\frac{NP_{max}}{\alpha I_{opt}}\right)I + \frac{NP_{max}}{\alpha}} \qquad\qquad [2]$$

319 Where $NP(I)$ is the rate of net primary production at light intensity, I, NP_{max} is the

320 maximum rate of NP at the optimal light intensity, I_{opt}, and α is the rate in which NP

321 increases up to NP_{max}.

322 Light saturated gross primary production (P) was then calculated for each assay temperature

323 as:

324 $$P = NP_{max} + R \qquad\qquad [3]$$

325 To investigate the effect of light limitation on the temperature dependence of photosynthesis

326 we used Eq. 2 to determine the predicted NP at half the light saturated irradiance (0.5 $\times$

327 I_{opt}). Thus replacing in NP_{max} in Eq. 3 with this prediction we derived $P_{0.5}$, a light limited

328 value of gross primary production at half the saturating irradiance for each assay temperature

329 response.

330 Metabolic rates were then converted from units $\mu mol \; O_2 \; mL^{-1} \; s^{-1}$ to $\mu g \; C \; \mu g \; C^{-1} \; hour^{-1}$. We

331 achieved this using the following equation:

332 $$b(\mu g\ C\ \mu g\ C^{-1}\ h^{-1}) = \frac{b(\mu mol\ O_2\ cell^{-1}\ h^{-1}) \times 32 \times M \times \left(\frac{12}{44}\right)}{\mu gC\ cell^{-1}} \qquad [4]$$

333 Where b is the metabolic rate (either P or R), 32 is the molecular weight of O_2, M is a species

334 specific assimilation quotient for $CO_2:O_2$ (35) which is used to describe consumption or

335 fixation of C in the cell per unit of O_2, and 12/44 is the ratio of molecular weight of C to CO_2,

336 thus $32 \times M \times \frac{12}{44}$ converts from $\mu mol\ O_2$ to μgC. Samples from each strain were analysed

337 to determine species-specific $\mu g\ C\ cell^{-1}$ values and the number of cells mL^{-1} was

338 measured for each biological replicate using flow cytometry. The calculation of M is based

339 on the assumption that NO_3^- is the main nitrogen source in the growth medium and that there

340 is a balanced growth equation, where:

341 $$nCO_2 + (n+1)H_2O + HNO_3 \rightarrow (CH_2O)_n\ NH_3 + (n+2)O_2 \qquad [5]$$
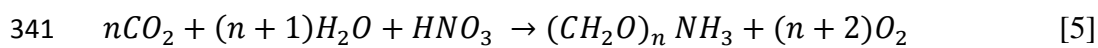
342 If the $C:N$ ratio (n) of the phytoplankton is calculated in moles then the ratio of $CO_2:O_2$, or M,

343 will be equal to $n/n+2$ (35). Our calculated values of M ranged from ~0.71 to ~0.89 (Table 3,

344 SI).

345 **Quantifying the thermal response curves**

346 The thermal response curves for rates of growth, photosynthesis (at both saturated and half

347 saturated irradiance) and respiration were quantified using a modified version of the Sharpe-

348 Schoolfield equation (12, 13):

349 $$\ln(b(T)) = E_a\left(\frac{1}{kT_c} - \frac{1}{kT}\right) + \ln(b(T_c)) - \ln\left(1 + e^{E_h\left(\frac{1}{kT_h} - \frac{1}{kT}\right)}\right) \qquad [6]$$

350 where b is either the rate of growth (d^{-1}), photosynthesis or respiration ($\mu g\ C\ \mu g\ C^{-1}\ h^{-1}$), k is

351 Boltzmann's constant (8.62×10^{-5} eV K^{-1}), E_a is the activation energy (eV), indicative of the

352 steepness of the slope leading up to the thermal optima, T is temperature in Kelvin (K), E_h is

353 the deactivation energy which characterizes temperature-induced decrease in rates above T_h

354 where half the enzymes have become non-functional and $b(T_c)$ is rate normalized to an

355 arbitrary reference temperature, here $T_c = 20°C$ (+ 273.15), where no low or high temperature

356 inactivation is experienced. Eq. 6 can be used to derive an optimum temperature where the

357 maximum rate is predicted:

358 $$T_{opt} = \frac{E_h T_h}{E_h + kT_h \ln\left(\frac{E_h}{E_a} - 1\right)} \qquad [7]$$

359 The parameters $b(T_c)$, E_a, E_h, T_h, and T_{opt}, can be considered as traits that characterise the

360 unimodal response of biological rates to temperature change. We expect these traits to differ

361 across the diverse taxa analysed in this study, owing to their diverse evolutionary histories

362 and ancestral temperature regimes (given that they have been isolated from different

363 latitudes/oceans). To test this assumption, we fitted the data for growth, photosynthesis and

364 respiration across all species to Eq. 6 using non-linear mixed effects modelling with the

365 'nlme' package in R. We used separate analyses to assess the thermal responses of growth,

366 photosynthesis and respiration. All models included each of the parameters in Eq. 6 as fixed

367 effects, which quantify the average value of the parameter across all species and replicates.

368 For the analysis of the thermal response of growth rate, we included 'species' as a random

369 effect on each parameter, which quantifies species-specific deviations from the average

370 across all species (i.e. the fixed effect) that are assumed to be normally distributed with a

371 mean of zero. For the analyses of photosynthesis and respiration, we included 'replicate'

372 nested within 'species' to account for the fact that we measured a minimum 3 replicate

373 thermal response curves for each species. Here the random effect quantifies species-specific

374 deviations from the fixed effects as well as those attributable to variance among the replicates

375 of each species.

376 Because the Sharpe-Schoolfield equation can only take non-zero and positive rate values, in

377 instances where either no observed growth rate, or a negative growth rate were measured

378 (typically the highest and lowest temperature) we set the rate to the minimum value measured

379 for the species in order to fit the model.

380

381 **Quantifying the carbon-use efficiency and modelling the break-point temperature**

382 The carbon-use efficiency (CUE) was calculated as:

383 $$CUE = 1 - R/P \qquad [8]$$

384 Due to the non-linear temperature response of the CUE, with accelerated declines at high-

385 temperatures, we fitted a segmented linear regression model to estimate the break-point in the

386 temperature response after which the CUE exhibited an accelerated decline. We fitted the

387 segmented linear regression model to CUE values derived from the fitted Sharpe-Schoolfield

388 curves for each species enabling us to derive an estimate of CUE at every 1°C increment

389 across the range of assay temperatures where metabolic rates were measured for each species

390   (Fig 2. Main text). We fitted the break-point model to the CUE values using the 'segmented'

391   package in R, where the breakpoint estimate is defined in the segmented model as the

392   intersection where there is significant difference in slopes (36), determined by the Davies test

393   for performing hypothesis (37). It is for this reason that it was necessary to use the predicted

394   values of respiration and photosynthesis to derive the break-point, as the measured data in

395   most cases only provided one or two data points beyond the inflection point, and this would

396   not have been sufficient to accurately model the second slope beyond this point (Fig.3, Main

397   text). The model returned an estimate of the CUE break-point temperature and the 95%

398   confidence intervals surrounding this value for each species (Table 7, SI).

Determining the temperature dependence of the CUE

400   We characterized the temperature dependence of the CUE up to the CUE breakpoint

401   temperature for each species using the Arrhenius equation,

402   $$\ln \text{CUE}(T) = E_a^{CUE}\left(\frac{1}{kT_c} - \frac{1}{kT}\right) + \ln \text{CUE}(T_c) \qquad [9]$$

403   where $\ln \text{CUE}(T)$ is the natural logarithm of the CUE at temperature T (in Kelvin), E_a^{CUE} is

404   the apparent activation energy characterising the temperature dependence of CUE. We

405   centred the temperature data using an arbitrary reference temperature $T_c = 283$ K = 20ºC, so

406   that $\ln \text{CUE}(T_c)$ is the CUE at T_c. We fitted Eq. 9 to all the measurements of CUE, up to the

407   CUE break-point temperature identified for each species (Fig.3 Main text, Table 7, SI) using

408   a linear mixed effects model. This allowed us to derive an average value for E_a^{CUE} and

409   $\ln \text{CUE}(T_c)$ across the 18 species. We also included random effects of 'replicate' nested

410   within 'species' in the model to account for the fact we measured a minimum of 3 replicate

411   responses of respiration and photosynthesis for each species. This allowed us to capture the

412   species-specific and replicate specific estimates E_a^{CUE} and $\ln \text{CUE}(T_c)$.

Acknowledgements

### Author contributions

417   S.B. and G.Y.-D conceived the study. S.B., G.Y.-D, A.B. and N.S. designed the experimental

418   work. S.B., J.J. and C.-E.S. conducted the experimental work. S.B. and G.Y.-D analysed the

419   data. S.B. and G.Y.-D wrote the manuscript and all authors contributed to revisions.

References

1. Henson S A, et al. (2017) Rapid emergence of climate change in environmental drivers of marine ecosystems. *Nat Commun* 8(5020):1–9.

2. Rhein, M. *et al.*(2013) Observations: Ocean Pages. *Climate Change 2013: The Phyical. Science Basis. Contribution to Working Group I to the Fifth Assessment Report of the Intergovernmental Panel on Climate Change,* Cambridge University Press, Cambridge, UK and New York, pp 255–316.

3. Collins, M. *et al.*(2013) Long-term Climate Change: Projections, Commitments and Irreversibility. *Climate Change 2013: The Phyical. Science Basis. Contribution to Working Group I to the Fifth Assessment Report of the Intergovernmental Panel on Climate Change,* Cambridge University Press, Cambridge, UK and New York, pp 1029–1136.

4. Boyce DG, Lewis MR, Worm B (2010) Global phytoplankton decline over the past century. *Nature* 466(7306):591–596.

5. Behrenfeld MJ, et al. (2006) Climate-driven trends in contemporary ocean productivity. *Nature* 444(December):752–755.

6. Capuzzo E, et al. (2018) A decline in primary production in the North Sea over 25 years, associated with reductions in zooplankton abundance and fish stock recruitment. *Glob Chang Biol* 24:e352–e364.

7. Laufkotter C, et al. (2015) Drivers and uncertainties of future global marine primary production in marine ecosystem models. *Biogeosciences* 12:6955–6984.

8. Thomas MK, Kremer CT, Klausmeier C a., Litchman E (2012) A Global Pattern of Thermal Adaptation in Marine Phytoplankton. *Science* 338:1085–1088.

9. Thomas MK, Kremer CT, Litchman E (2016) Environment and evolutionary history determine the global biogeography of phytoplankton temperature traits. *Glob Ecol Biogeogr* 25:75–86.

10. Falkowski PG, et al. (2004) The Evolution of Modern Eukaryotic. *Science* 305:354–360.

11. Keeling PJ (2004) Diversity and evolutionary history of plastids and their hosts. *Am J Bot* 91(10):1481–1493.

12. Sharpe, PJH, DeMichele, DW (1977) Reaction Kinetics of Poikilotherm Development. *J. Theor. Biol.* 64, 649–670 .

13. Schoolfield RM, Sharpe PJH, Magnuson CE (1981) Non-linear regression of biological temperature-dependent rate models based on absolute reaction-rate theory. *J Theor Biol* 88:719–731.

14. Eppley RW (1972) Temperature and phytoplankton growth in the sea. *Fish Bull* 70(4):1063–1085.

455   15.   Chen B, Laws E a. (2017) Is there a difference of temperature sensitivity between marine
456   phytoplankton and heterotrophs? *Limnol Oceanogr* 62:806–817.

457   16.   Kremer CT, Thomas MK, Litchman E (2017) Temperature- and size-scaling of phytoplankton
458   population growth rates: Reconciling the Eppley curve and the metabolic theory of ecology.
459   *Limnol Oceanogr* 62:1658–1670.

460   17.   Quigg A, et al. (2003) The evolutionary inheritance of elemental stoichiometry in marine
461   phytoplankton. *Nature* 425(6955):291–4.

462   18.   Shuter B (1979) A model of physiological adaption in unicellular algae. *J Theor Biol* 78:519–
463   552.

464   19.   Raven J A., Geider RJ (1988) Temperature and algal growth. *New Phytol* 110:441–461.

465   20.   Raven J A (1976) The Quantitative Role of ' Dark ' Respiratory Processes in Heterotrophic
466   and Photolithotrophic Plant Growth. *Ann. Bot.* 40:587–602.

467   21.   Geider RJ, Osborne B A (1989) Respiration and microalgal growth : a review of the
468   quantitative relationship. *New Phytol* 112:327–341.

469   22.   Padfield D, Yvon-Durocher G, Buckling A, Jennings S, Yvon-Durocher G (2016) Rapid
470   evolution of metabolic traits explains thermal adaptation in phytoplankton. *Ecol Lett* 19:133–
471   142.

472   23.   Schaum C-E, Buckling A, Smirnoff N, Studholme DJ, Yvon-Durocher G (2018)
473   Environmental fluctuations accelerate molecular evolution of thermal tolerance in a marine
474   diatom. *Nat Commun*:1–14.

475   24.   Schaum C-E, et al. (2017) Adaptation of phytoplankton to a decade of experimental warming
476   linked to increased photosynthesis. *Nat Ecol Evol* 1:0094.

477   25.   Marañón E, Lorenzo MP, Cermeño P, Mouriño-Carballido B (2018) Nutrient limitation
478   suppresses the temperature dependence of phytoplankton metabolic rates. *ISME J*.
479   doi:10.1038/s41396-018-0105-1.

480   26.   Moore CM, et al. (2013) Processes and patterns of oceanic nutrient limitation. *Nat Geosci*
481   6(9):701–710.

482   27.   Bruland KW, Rue EL, Smith GJ, DiTullio GR (2005) Iron, macronutrients and diatom blooms
483   in the Peru upwelling regime: Brown and blue waters of Peru. *Mar Chem* 93:81–103.

484   28.   Townesend DW, Cammen LM, Holligan PM, Campbell DE, Pettigrew NR (1994) Causes and
485   consequences of variability in the timing of phytoplankton blooms. *Deep Res Part I*
486   41(5):747–765.

487   29.   Pingree RD, Pugh PR, Holligan PM, Forster (1975) Summer phytoplankton blooms and red
488   tides along tidal fronts in the approaches to the English Channel. *Nature* 258:672–677.

489   30.   Baranyi J, Roberts T a. (1994) A dynamic approach to predicting bacterial growth in food. *Int*
490   *J Food Microbiol* 23:277–294.

491   31.   Raven J A (1976) The Quantitative Role of ' Dark ' Respiratory Processes in Heterotrophic
492   and Photolithotrophic Plant Growth. *Ann. Bot.* 40:587–602.

493   32.   Ho T, et al. (2003) the Elemental Composition of Some Marine Phytoplankton. *J Phycol*
494   39:1145–1159.

495   33.   Eilers PHC, Peeters JCH (1988) A model for the relationship between light intensity and the
496   rate of photosynthesis in phytoplankton. *Ecol Modell* 42:199–215.

497   34.   Edwards KF, Thomas MK, Klausmeier C a., Litchman E (2016) Phytoplankton growth and the
498   interaction of light and temperature: A synthesis at the species and community level. *Limnol*
499   *Oceanogr* 61:1232–1244.

500   35.   Falkowski PG, Gan R, Wyman K (1985) Growth-irradiance relationships in phytoplankton .
501   *Limnol. Oceanogr.* 30(2):311–321.

502   36.   Muggeo VMR (2003) Estimating regression models with unknown break-points. *Stat Med*
503   22:3055–3071.

504   37.   Davies RB (1977) Hypothesis Testing when a Nuisance Parameter is Unidentified Under the
505   Alternative. *Biometrika* 64:247–254.

506

507
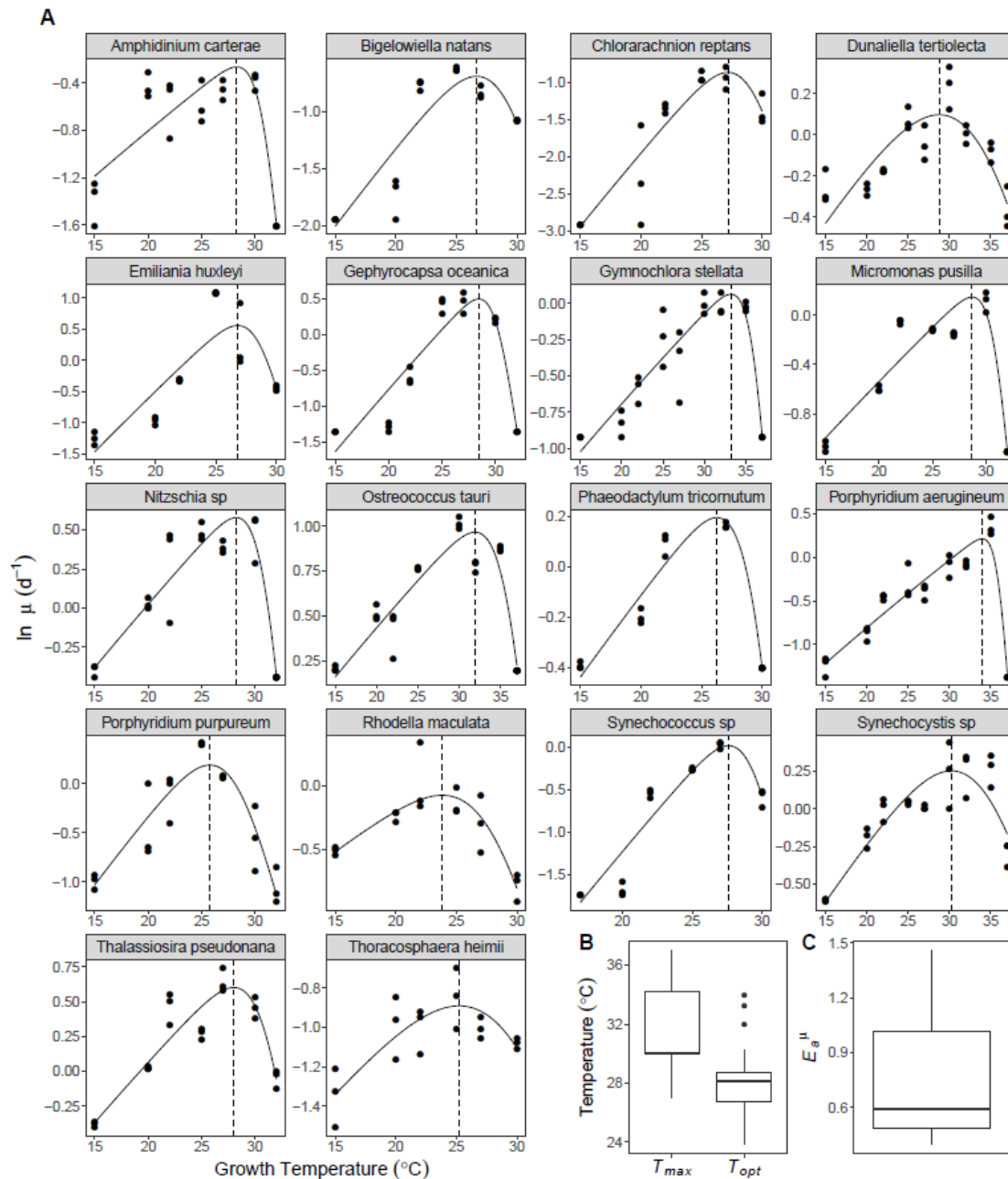
Fig. 1. Thermal tolerance curves for 18 species of marine phytoplankton. (A) Thermal reaction norms for all 18 species used in this study. The data points presented are the natural logarithm of per capita growth rate, μ, for each replicate (n= minimum of 3 technical replicates per assay temperature for each species). The fitted lines are from the predicted random effect of species derived from non-linear mixed effects modelling with a Sharpe-Schoolfield model. The vertical dashed lines correspond with the optimal temperatures of growth. **(B)** Boxplot distributions of optimal growth temperatures (T_{opt}) and maximum temperatures of growth (T_{max}) across all 18 species. **(C)** Boxplot distribution of growth activation energy, or temperature dependence (E_a^{μ}), across all 18 species (Table 2, SI). The bold horizontal line corresponds to the median value, the top and bottom of the box correspond to the 75th and 25th percentiles and the whiskers extend to the largest and smallest values no greater or less than 1.5 $\times$ the interquartile range, beyond which the points are plotted as outliers.
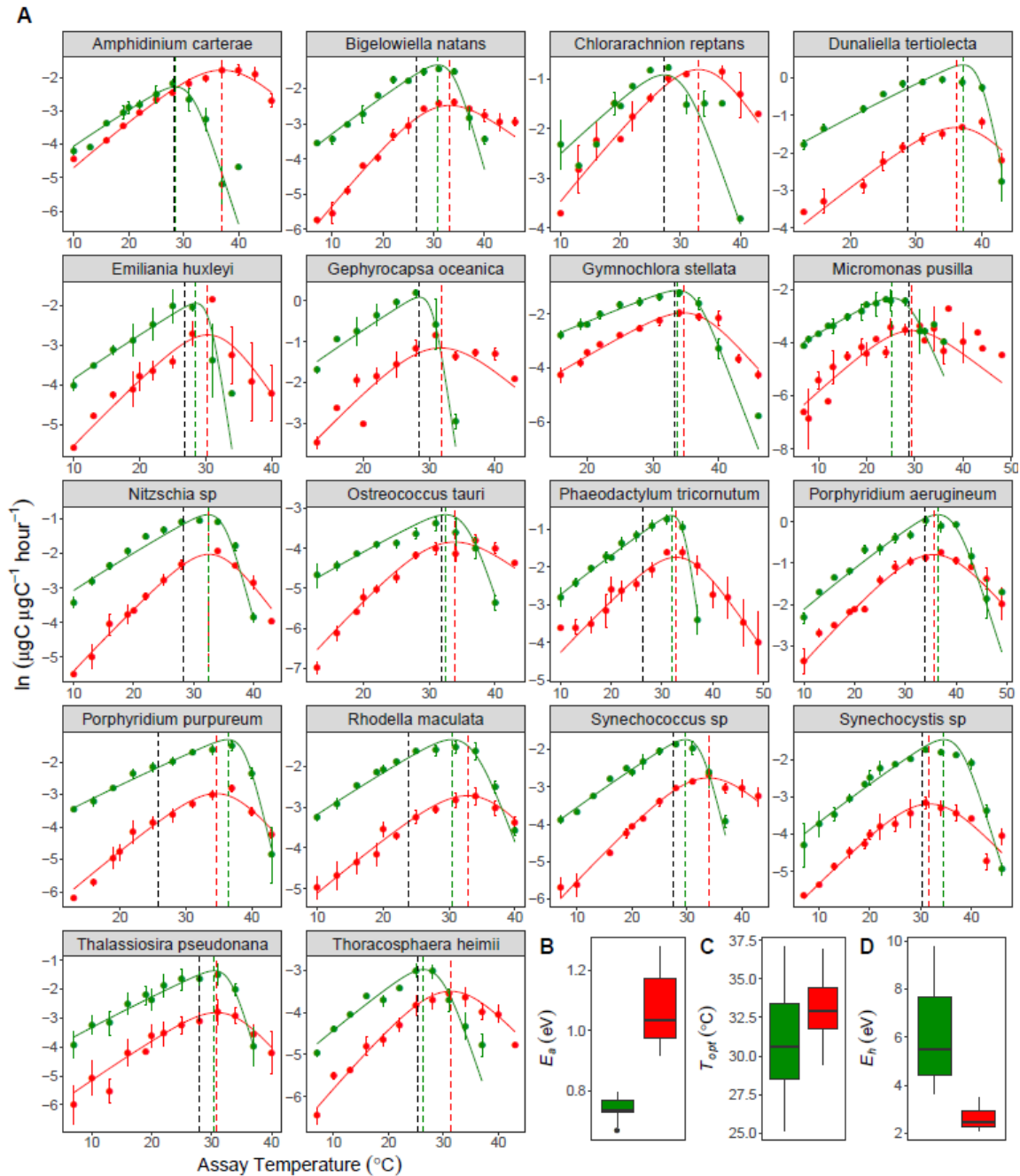
Fig. 2. Thermal performance curves for respiration and gross photosynthesis in 18 species of marine phytoplankton. (A) Metabolic thermal performance curves for all 18 species used in this study. Green colouring denotes gross photosynthesis, red colouring denotes respiration. The data points presented are the natural logarithm of mean metabolic, with error bars denoting $\pm$ s.e.m (n = minimum of 3 biological replicates per response for each species). The fitted lines for each species are from the random effects of a non-linear mixed effects model fitted to the rate data using the Sharpe-Schoolfield equation (see Methods). The vertical dashed lines correspond with the optimal temperatures for each metabolic flux, with the black dashed line added to show optimal growth temperature. **(B, C and D)** Boxplots showing the distribution of the estimated values for activation energy (E_a), optimal temperature (T_{opt}) and deactivation energy (E_h) for photosynthesis and respiration across the 18 species (Tables 4 and 5, SI). The bold horizontal line corresponds to the median value, the top and bottom of the box correspond to the 75th and 25th percentiles and the whiskers extend to the largest and smallest values no greater or less than 1.5 $\times$ the interquartile range, beyond which the points are plotted as outliers.
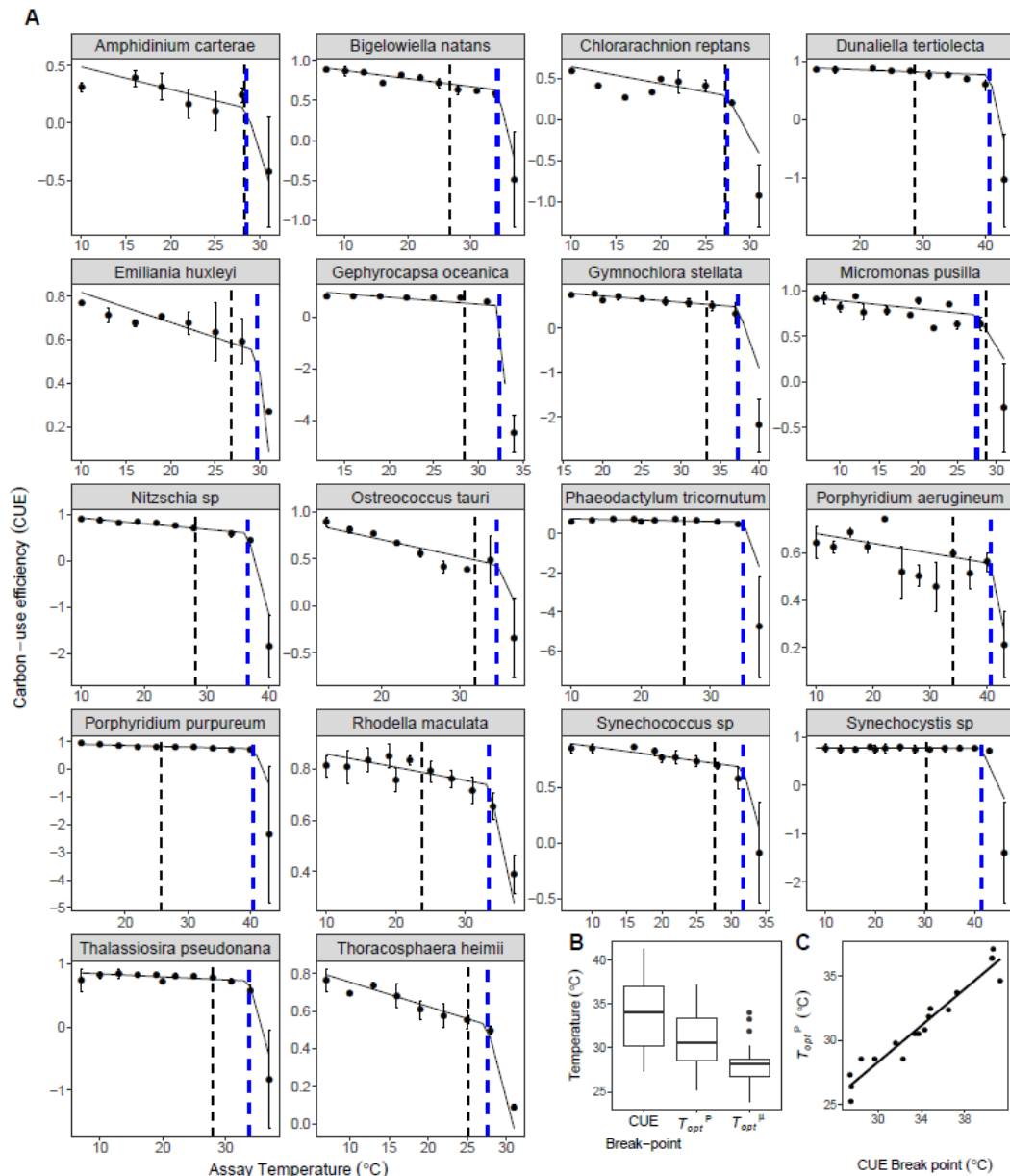
Figure. 3. Carbon-use efficiency breakpoints constrain the optimal temperature of growth. (A)
Segmented linear regression models fitted to the predicted carbon use efficiency (CUE), derived from the thermal performance parameters of respiration and photosynthesis for each species (Fig 2). The modelled response is presented here alongside the calculated mean CUE at each assay temperature, with with error bars denoting ± s.e.m (n = minimum of 3 biological replicates per response for each species). The dashed vertical dashed blue line represents the predicted break-point in the model, where there was a significant change in the slope of the CUE thermal response. The dashed vertical black line represents the estimate optimal temperature of growth (Fig.1). In most cases this either coincides with the break-point, falling within the 95% CIs of the break-point, or was lower than the break-point. **(B)** Boxplots showing the distribution of the estimated values for the CUE break-point temperature, optimal temperature of gross photosynthesis (T_{opt}^{P}) and optimal temperature of growth (T_{opt}^{μ}) across the 18 species (Tables 2, 4 and 5, SI). The bold horizontal line corresponds to the median value, the top and bottom of the box correspond to the 75th and 25th percentiles and the whiskers extend to the largest and smallest values no greater or less than 1.5 × the interquartile range, beyond which the points are plotted as outliers. **(C)** The significant coupling between the CUE and T_{opt}^{P}, illustrating that the sharp declines in CUE are determined by the universal metabolic constrains identified in Fig.2.
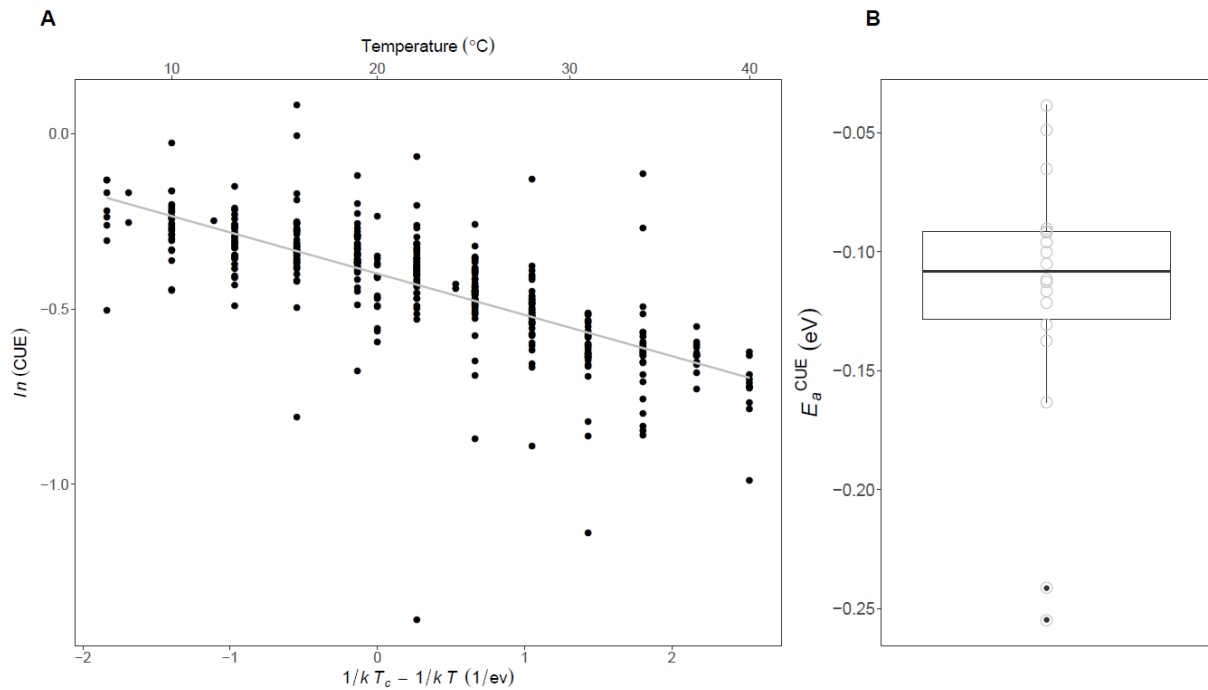
553

554 **Figure. 4. The temperature dependence of the carbon-use efficiency.** **(A)** A scatterplot showing
555 the relationship between the natural logarithm of the carbon-use efficiency (CUE) and standardised
556 Boltzmann temperature up to the CUE break-point (Fig.3) for the pooled dataset of 18 species, where
557 $T_c = 20°C$ and k is the Boltzmann constant (8.62×10^{-5} eV). The fitted line represents the fixed
558 effect of a linear mixed effects model fitted to the data using the Boltzmann-Arrhenius equation (see
559 Methods). Values of ln(CUE) have been standardised by dividing by the species-specific intercept
560 derived from the random effects of the mixed effects model. This standardisation was for visualisation
561 of the data only.   The plot demonstrates that the CUE decreases up to the CUE break-point
562 temperature with a consistent temperature dependence, equating to an average activation energy (
563 E_a^{CUE}) of -0.12eV. **(B)** Boxplot of the species-specific E_a^{CUE} values derived from the linear mixed
564 effects model. The bold horizontal line corresponds to the median value, the top and bottom of the
565 box correspond to the 75th and 25th percentiles and the whiskers extend to the largest and smallest
566 values no greater or less than 1.5 $\times$ the interquartile range, beyond which the points are plotted as
567 outliers.

568

569

570